



Simulation and optimization of a sheathless size-based acoustic particle separator

Shivaraman Asoda¹ · Rasim Guldiken¹

Received: 7 August 2018 / Accepted: 27 September 2018 / Published online: 3 October 2018
© Springer-Verlag GmbH Germany, part of Springer Nature 2018

Abstract

Standing surface acoustic waves (SSAW) have been widely used for sorting of particles and cells. However, the challenge with the acoustic driven separation process is the need for an optimized setup to achieve effective separation and the range of particles that can be separated. In this study, we present our findings on a custom simulation model to investigate and optimize the separation of varying size particles in a sheathless acoustic separation platform that was developed in our research lab. Specifically, we investigate the effect of flowrate, pressure amplitude, wavelength and interdigitated transducers physical parameters on the separation efficiency. We also explored the critical particle size for acoustic particle separation with 3 μm particles and demonstrated, successful 3 μm and 6 μm particles for the first time for this sheathless separation platform. The ANSYS[®] FLUENT was used to numerically simulate acoustic radiation force on the particles for separation. With the increase in the pressure amplitude in the first and second stage to 80 kPa and 110 kPa respectively, the optimization studies presented have shown to improve the separation efficiency of the model over 96% for both 10 and 3 μm particles. Findings of the present study will aid in increasing the efficiency of particle separation and in designing the SSAW driven microfluidic devices.

1 Introduction

Isolating specific cells is a crucial step in many techniques used in the area of biology and related disciplines. In biomedical applications, effective cell sorting is required for understanding the cells function and their response to stimuli (Plouffe et al. 2015). Use of sorted cells reduces the heterogeneity of the study sample and decreases the variations among the experiments. Some of the representative examples in biomedicine where separation techniques employed are: sorting out malaria infected cells for diagnostics, isolation of platelets and separation of circulating tumor cells from the blood (Plouffe et al. 2015; Guldiken et al. 2012; Jo and Guldiken 2012, 2013).

Numerous sorting techniques have been developed based upon the physical properties of the cell such as size,

density, electrical or magnetic affinity etc. (Plouffe et al. 2015; Jo and Guldiken 2012). Standard separation techniques such as filtration, centrifugation and sedimentation can be used for the separation of cells (Plouffe et al. 2015). In cases where the cell size or density difference are not significant, the efficiency of the cell separation is lower. In such cases, acoustic based cell separation techniques may be employed to acquire higher cell sorting efficiency.

In acoustic based cell separation technique, microfluidic separation is achieved by applying differential forces on target cells to guide them into different paths. This is the only active separation technique that can distinguish cells based on their size, density and compressibility (Li et al. 2015). As this method requires the application of external acoustic forces, the separation performance can be controlled to accommodate the separation of different cell samples with distinct physical properties (Guo et al. 2016). Compared to other standard cell sorting techniques, acoustic-based manipulations have been recognized as more biocompatible (Ding et al. 2013). Acoustic based approaches thus offer excellent alternatives for cell separation and have potential to aid in cancer research, therapeutics and drug efficacy assessment (Li et al. 2015).

✉ Rasim Guldiken
guldiken@usf.edu
Shivaraman Asoda
shivaraman@mail.usf.edu

¹ Department of Mechanical Engineering, University of South Florida, 4202 E. Fowler Avenue, ENB 118, Tampa, FL 33620, USA

In this work, we present an advanced simulation study of cell sorting technique that is based on a tunable standing surface acoustic waves (SSAW). In SSAW-based cell sorting, cells experience acoustic radiation force directly rather than using the acoustic streaming effect which manipulate the fluids in which the cells are present (Ding et al. 2012). This method can define and change the pressure nodes (PNs) of SSAW and thus guide the cells into different paths (and into the designated outlets). This method can achieve more controlled and stable cell manipulation when compared to acoustic-streaming-based approaches which is often unpredictable (Ding et al. 2012). In addition, this method can produce a large range of translation and it is capable of precisely sorting cells into a great number of outlet channels (e.g. four) in a single step (Ding et al. 2012). This provides a significant advantage over many existing cell-sorting methods, which typically separate the cells into two outlets. However, for efficient separation, positioning of the PNs/ANs (pressure anti nodes) is required depending upon the design of the microchannel. This can be achieved through the generation of tunable SSAW using interdigital transducers (IDTs). Hence, by tuning the frequency of SSAW, we can move the PNs/ANs in the lateral direction normal to the cell flow, which in turn drives the cells to their designated outlets (Ding et al. 2012).

In this study, we developed a simulation model that demonstrates particle separation by acoustic radiation force and has the ability to simulate the particles of different physical properties. We also performed systematic parametric studies of the factors influencing the separation efficiency of the model and explore the merits of utilizing alternate designs to optimize the separation efficiency. Although this study concentrates on the separation of polystyrene particle, it can also be extended for particles of any type.

2 Acoustic radiation force

The radiation force experienced by an object in the presence of acoustic field is known as acoustic radiation force (ARF) (Hu 2013). Acoustic radiation force can be used to manipulate the particle trajectories by moving them towards the nodal (or anti-nodal) positions in an acoustic field depending upon their material properties. Utilizing this principle, various acoustic based separators have been investigated for biomedical and chemical analysis. For generating acoustic standing wave field, either surface acoustic waves (SAWs) or bulk acoustic waves (BAWs) can be used in microfluidic devices (Liu et al. 2017; Zhang et al. 2014). In this study we adopt a method of using SSAW for continuous particle separation in a microfluidic

channel. Using this method, particles in a continuous flow can be separated based on their compressibility, density and volume (Shi et al. 2009).

The investigation of acoustic radiation force on suspended particles have a long history. The analysis of acoustic radiation force on incompressible spheres was done by King (1934), while the forces on compressible spheres were calculated by Yosioka and Kawasima (1955). ARF (F_r) induced on a particle present in an acoustic standing wave field in a compressible medium is given by Yosioka and Kawasima (1955),

$$F_r = -\frac{(\pi p_o^2 V \beta_m)}{2\lambda} \varphi(\beta, \rho) \sin(2kx) \quad (1)$$

$$\varphi(\beta, \rho) = \frac{(5\rho_p - 2\rho_m)}{(2\rho_p + \rho_m)} - \frac{\beta_p}{\beta_m} \quad (2)$$

where V , λ , β , ρ are the particle's volume, wavelength, compressibility, density while k , x , p_o , φ are the wavenumber, distance from the pressure node, acoustic pressure amplitude and acoustic contrast factor respectively. The subscript of m and p represent the liquid medium and particle respectively.

Form Eq. 1, it can be seen that the ARF changes sinusoidally with an interval of a half wavelength in space. The displacement of the particle towards the pressure node or the pressure anti-node is determined by the acoustic contrast factor (φ): if $\varphi > 0$, the particles will gather at pressure nodes; if $\varphi < 0$, the particles will gather at antinodes (Laurell et al. 2007). It is noted that the force on a particle is proportional to the cube of particle radius and this indicates that the larger particles will experience higher force than the smaller particles.

The SSAW generator is basically a pair of interdigitated transducers (IDTs) fabricated on a piezoelectric substrate. A microchannel is set between two IDTs to form a microfluidic device. SAWs propagate in the opposite direction towards the microchannel when an AC signal is applied to the IDTs. Constructive interference of the two SAWs leads to the formation of SSAW field across the channel. The SSAW couples into the fluid medium and produces acoustic radiation force on the particles suspended in the liquid. The change in the trajectory of a particle towards PNs or ANs is determined by the density and the compressibility of the particle and the surrounding medium. However, most solid particles suspended in aqueous solution, including cells move towards the pressure nodes (Laurell et al. 2007).

The simulation work performed in this study is based on a sheathless size-based acoustic particle separation design that was experimentally investigated previously (Guldiken et al. 2012). In the exploratory work carried out, four IDTs with a rectangular component design are utilized to

generate acoustic standing wave fields. The IDT finger width and finger pitch were picked as 75 μm and 300 μm respectively. A pair of IDTs of sizes 7.7 mm \times 6 mm and 1.7 mm \times 6 mm were fabricated on lithium niobate substrate in the first stage and second stage respectively as shown in Fig. 1.

The microchannel is fabricated on the substrate such that it is located on the center line between the IDTs and the SAW wavelength was chosen to be 300 μm . Figure 2 illustrates the design concept of a two-stage SSAW particle separator. For the first stage, the width of the microchannel has been designed to be equivalent to half of the wavelength of the SSAW. The design promotes the aggregation of the particles at the micro-channel centerline, before they enter the second stage. In order to have the two off-center pressure nodes, the second stage microchannel width was taken to be that of one full wavelength. As the particles travel in the second stage of the design across the microchannel, acoustic forces are experienced by the particles towards the pressure nodes. Depending on the material properties, the unlike particles experience different acoustic forces leading them to follow different trajectories. Therefore, variation in material properties of these particles results in their subsequent segregation.

The solution mixture used for separation involved polystyrene fluorescent particles ($\rho = 1.05 \text{ g/cm}^3$ and $\beta = 2.46\text{e}-10 \text{ Pa}^{-1}$) with diameter 3 μm and 10 μm and were infused into the microchannel by a syringe pump. The acquired high-speed images of the fluorescence in the microchannel were used to observe the particle segregation in the acoustic standing wave fields in DI-water medium

($\rho = 1.0 \text{ g/cm}^3$ and $\beta = 4.58\text{e}-10 \text{ Pa}^{-1}$). From the experimental measurements, it was observed that the fluorescent particles in the DI-water medium were effectively isolated with high efficiency and the sheathless SSAW based particle separation has been accomplished.

The present work is performed to further support the experimental data by using numerical simulations. A commercially available finite element modeling software—ANSYS® Fluent—is used to simulate particle velocity distribution, acoustic radiation force and particle patterning process. The present study not only considers the separation of same particles of two different sizes, but also examines the merits of utilizing alternate designs to optimize the separation efficiency.

3 Simulation work

Recent developments in the field of numerical simulation enabled Computational Fluid Dynamics (CFD) an effective method to reveal the properties of the fluid flow. They provide fast and flexible methods for solving engineering problems at low cost. Incorporating the simulations in biomedicine has led to the better understanding of various phenomena like blood flow in deformable vessels (Xiong et al. 2011), assessing the growth rate of tumors (Chen et al. 2015) etc. As a result, the application of CFD in biomedicine industry have gradually increased over the past few years. In this study, the commercial software ANSYS® 18.1 was used for designing and simulating the fluid flow in the microchannel.

Fig. 1 **a** Fabricated IDTs patterned on a lithium niobate wafer; **b** microchannel mold; **c** acoustic particle separator (Guldiken et al. 2012)

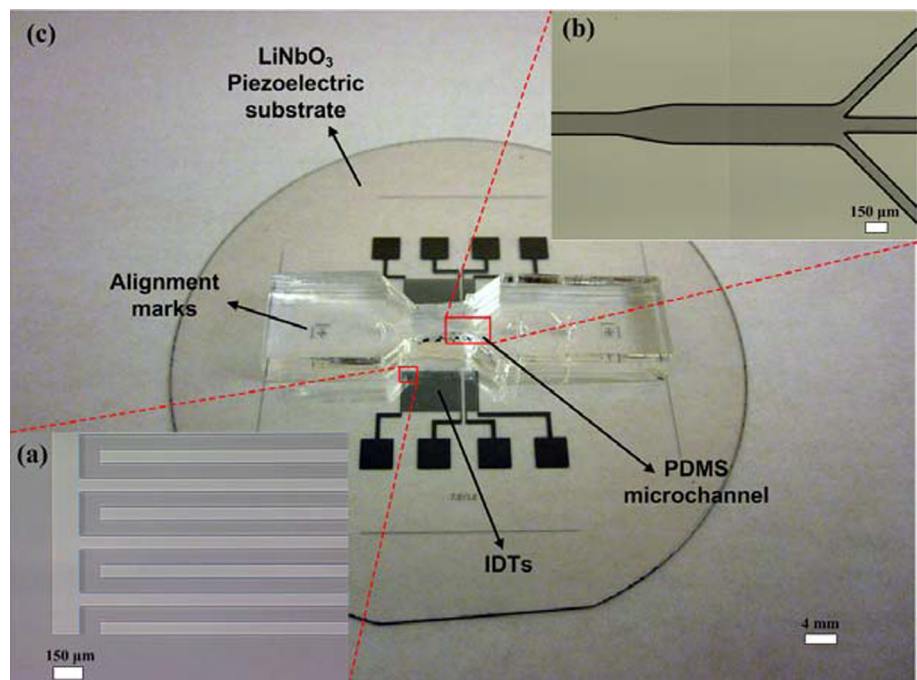
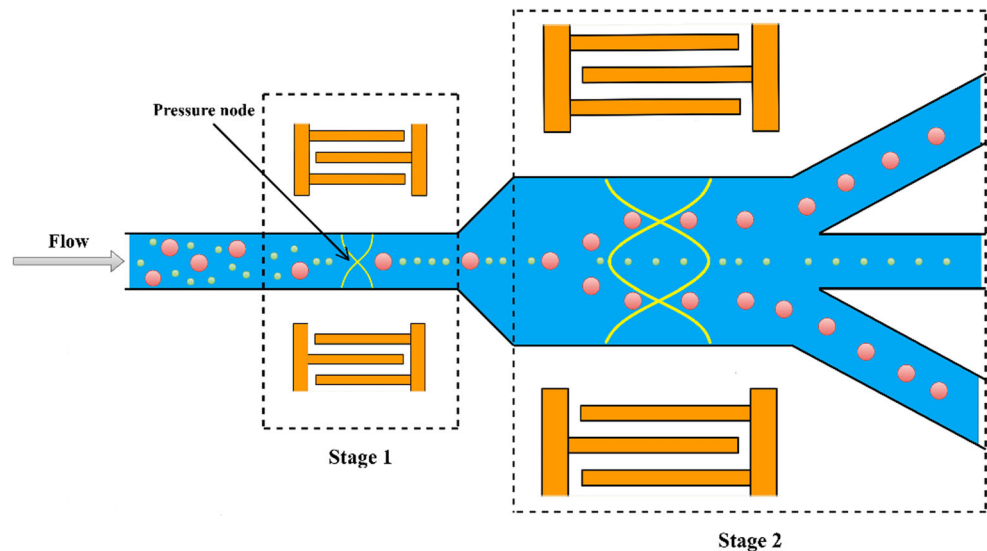


Fig. 2 Conceptual view of SSAW particle separator (Guldiken et al. 2012)



Based on the concept of a two-stage SSAW particle separator, a geometric model illustrated in Fig. 3 was established by using ANSYS DesignModeler. The length of the first microchannel and second microchannel are 11.81 mm (0.46 in.) and 5.67 mm (0.22 in.) respectively. The model has a single inlet and three outlets. The first channel has a width of 0.15 mm (0.006 in.) and the second stage microchannel width is taken as 0.3 mm (0.012 in.). The depth of the channel is 0.1 mm (0.004 in.) and is maintained uniform throughout the flow.

In this study, mesh for the simulation model is generated by performing edge sizing along the length, width and height of the model. As a result, the generated mesh contains of 125,048 nodes and 98,490 elements. ANSYS specifies that skewness of less than 0.25 and an orthogonal quality of 0.95 are considered excellent (ANSYS® Academic Research 2017). For the model designed, the average orthogonal quality and the average skewness of the cells generated are 0.99306 and 4.6509e–002, respectively as illustrated in Table 1. The maximum aspect ratio of the

Table 1 Mesh metrics for the designed model

Mesh metric	Obtained	Ideal range
Orthogonal quality	0.99306	0.95–1
Aspect ratio	7.5323	< 10
Skewness	4.6509e–02	> 0–0.25

mesh is 7.5323 which is within the acceptable limits, as the ANSYS guide specifies that the quadrilateral/hexahedral/wedge cells inside the boundary layer can have the aspect ratio of up to 10:1 in most cases. With regard to the stability of the flow solution, aspect ratio can go as high as possible. However, the maximum aspect ratio should be kept below 35:1 (ANSYS® Academic Research 2017).

An ANSYS Fluent model was developed based upon the boundary conditions as observed from the experimental setup of the sheathless size based acoustic particle separation (Guldiken et al. 2012). For all the cases analyzed, a

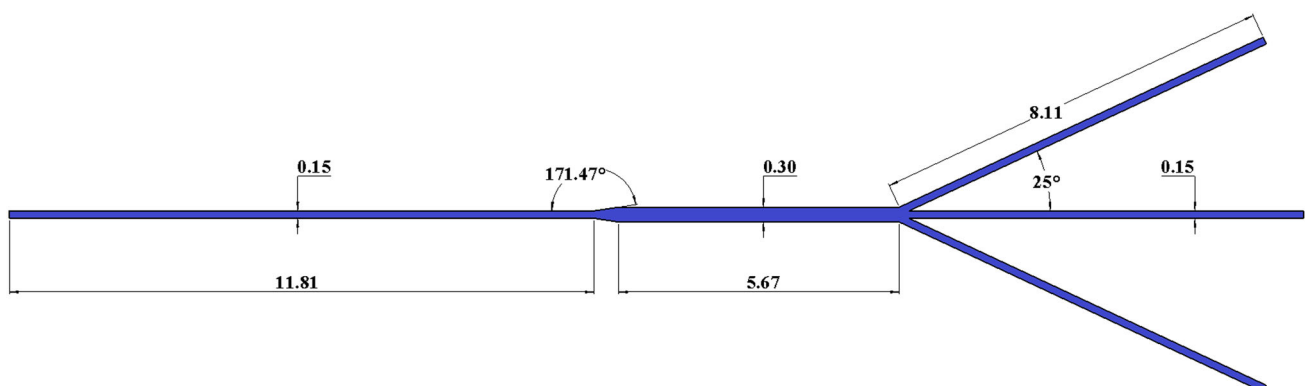


Fig. 3 Microfluidic channel of SSAW particle separator (dimensions in mm)

laminar viscous model with fluid as DI-water medium ($\rho = 1.0 \text{ g/cm}^3$) and particles as polyester fluorescent particles ($\rho = 1.05 \text{ g/cm}^3$) were used for simulating the acoustic separation process. The boundary conditions have been derived from the experimental setup. An experimental average inlet mass flow rate of $8.33\text{e}^{-09} \text{ kg/s}$ was taken as inlet boundary condition while the outlet gauge pressure has been taken to be 0 kPa. Reynolds number at the inlet has been found to be equal to 0.075 and the hydraulic diameter for the inlet was $1.2\text{e}^{-04} \text{ m}$.

In discrete phase modelling, surface type injection was selected at the inlet for introducing the particles into the fluid and face normal direction was used as the boundary condition. The body force experienced by the particles due to the acoustic radiation force, during their flow has been applied through a user defined function in discrete phase modeling. The simulation is then carried out for particles of different diameters by varying different parameters.

After the simulation, a step by step report of each injection was extracted from particle tracks with reporting variables as Particle Residence Time, Particle I.D, Particle Y Position, Particle X position and Particle Time step in order. The data obtained from the track history is then used as an input to a developed code to calculate the number of particles obtained at each outlet. The separation efficiency for the simulation is then calculated depending upon the number of particles at their respective outlets. To quantitatively evaluate the accuracy of the simulation, the time taken by the particles to reach to the pressure nodes in the first stage was compared and verified with the theoretical data.

When a particle in the SSAW field maintains a constant velocity, the time needed for its migration towards the respective pressure node which is at a distance δx in the range of $(0, \lambda/4)$ is given by the expression (Shi et al. 2009):

$$t = \left(\frac{3\lambda^2 \eta r_c}{\pi} \right) \left[\ln \tan \left(\frac{2\pi x}{\lambda} \right) \right]_{x_1}^{x_2} / [p_o^2 V_c \beta_w \theta(\rho, \beta)] \quad (3)$$

where $\lambda, \theta, \eta, \beta_w$ correspond to wavelength, acoustic contrast factor, viscosity, compressibility of the medium respectively and p_o, r_c, V_c correspond to pressure amplitude, particle radius and particle volume respectively.

For verification purposes, 16 particles having particle id's 0 to 15 were chosen from Fluent. These 16 particles were found to be randomly oriented around the center of the channel. Then the time taken for the particles to reach the pressure node in the first stage is estimated from the Fluent track history file. The results from the simulation is then compared with the theoretical data obtained from the Eq. (3). Figure 4 illustrates the deviation of simulated results from the theoretical data.

One can observe from Fig. 4 that the error in simulated results is less than 4% when compared with the theoretical values. As the accuracy of simulation is established, simulation work is then carried out for various parametric conditions.

4 Results and discussion

During the simulations the distribution of particles was captured at three different outlets represented as A, B and C as illustrated in Fig. 5. The separation efficiency of 3 μm particles was defined as $B/(A + B + C)$ and $(A + C)/(A + B + C)$ for the larger particles, where A, B and C are the number of particles obtained at the outlets A, B and C respectively.

4.1 Separation of 10 μm and 3 μm particles

During separation process, input wave length was taken as 300 μm and a constant pressure amplitude (I) of 100 kPa was applied in the first stage. An inlet mass flow rate was taken to be $8.33\text{e}^{-09} \text{ kg/s}$ as discussed in Sect. 3. Then the separation efficiency was calculated by varying the pressure amplitude (II) from 30 to 120 kPa in the second stage. The variation of separation efficiency obtained as a function of pressure amplitude in the second stage is illustrated in Fig. 6.

In the second stage, acoustic radiation force (ARF) on the particles increases with the increase in pressure amplitude as it is observed from Eq. 1 that ARF is directly proportional to the square of pressure amplitude (p_o). Due to this, as the pressure amplitude increases, quantity of 10 μm particles at their respective outlets increases but it also causes the 3 μm particles to deviate from its path resulting in a decrease in separation efficiency. This behavior of particles is illustrated in Fig. 6 when the pressure amplitude (II) is increased from 30 to 80 kPa. Also, as the pressure amplitude (II) increases to 80 kPa the variations in the separation efficiency of 10 μm particles is found to greater than that of 3 μm particles. This is because, 10 μm particles experiences an acoustic radiation force (ARF) 37 times than that of 3 μm particles due to their relatively large volume which in turn causes larger variations in separation efficiency.

From Fig. 6, it is observed that at an optimal pressure amplitude of 80 kPa, both the particles 10 μm and 3 μm have a separation efficiency of 100% and 86.67% respectively. The efficiency of 3 μm particles obtained can be further improved by increasing their concentration at the center of the channel. This can be attained by raising the pressure amplitude (I) in the first stage. The separation efficiency of particles obtained by varying the pressure

Fig. 4 Time taken for particles to reach pressure node

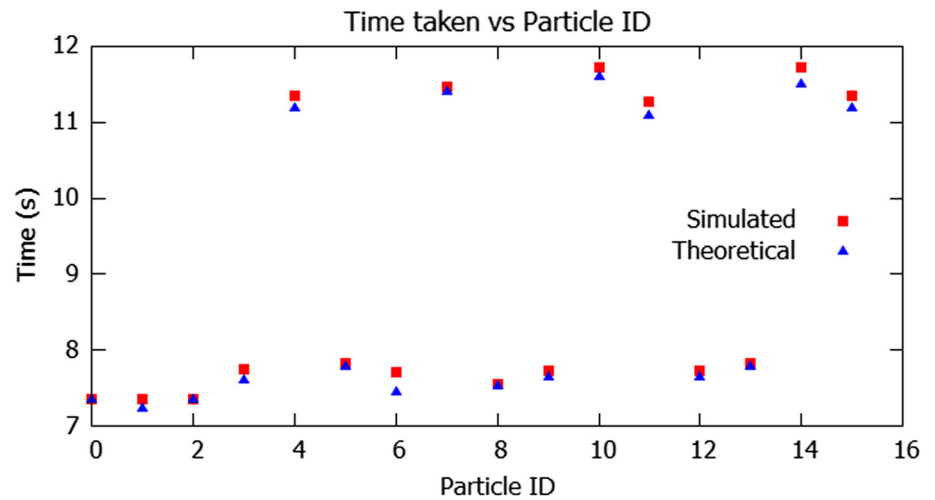


Fig. 5 The chosen outlets (A–C) in the microchannel for capturing the distribution of particles

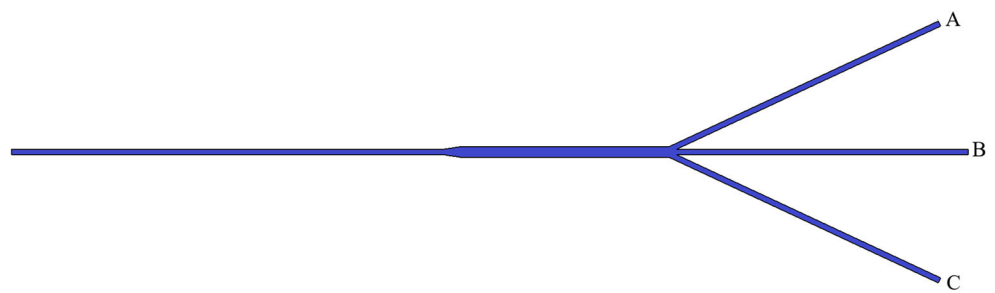
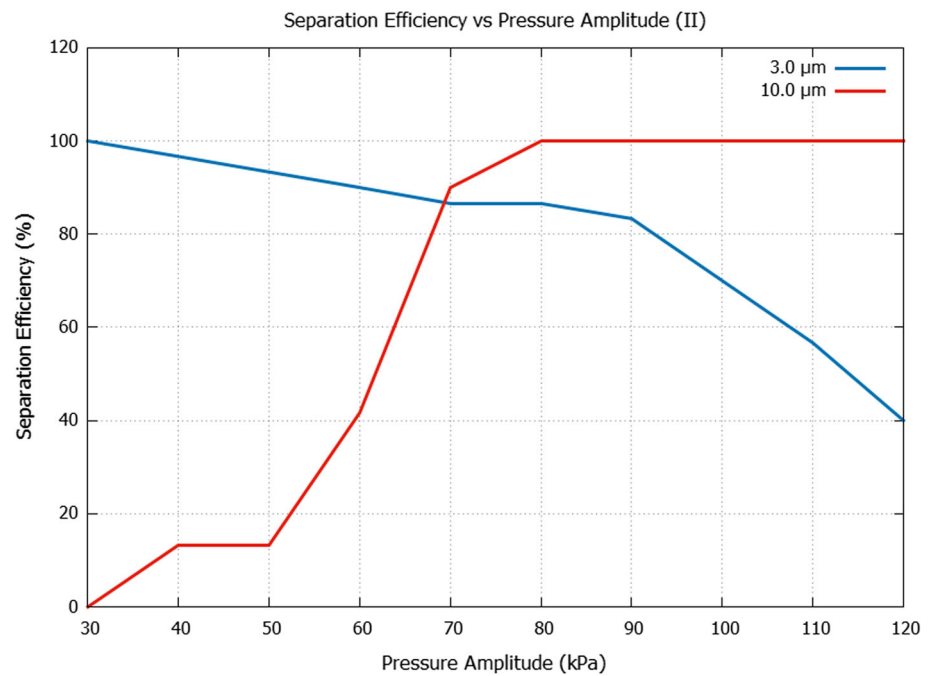


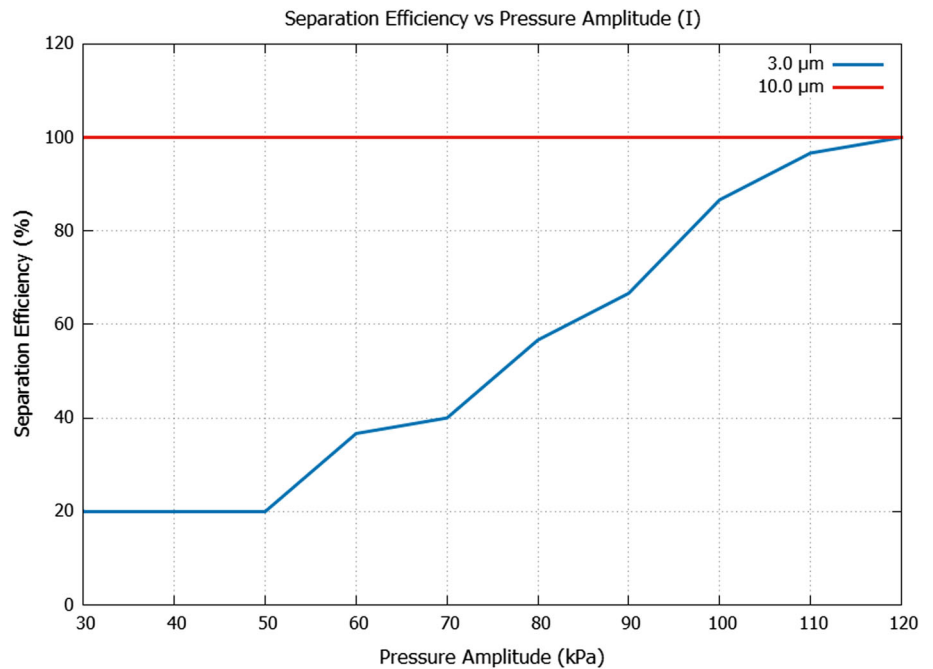
Fig. 6 Variation of separation efficiency with pressure amplitude (II)



amplitude (I) in the first stage is illustrated in Fig. 7. For this set of simulations, a constant pressure amplitude (II) of 80 kPa was applied in the second stage and the first stage pressure amplitude was varied from 30 to 130 kPa.

One can observe from Fig. 7 that as the pressure amplitude increases, the separation efficiency of 3 μm particles increases while the efficiency remains constant at 100% for 10 μm particles. This is because, even though the Pressure amplitude (I) is varied from 30 to 130 kPa, second

Fig. 7 Variation of separation efficiency with pressure amplitude (I)



stage pressure amplitude (II) is high enough to separate them effectively. At 110 kPa, both the particles 10 μm and 3 μm have a separation efficiency of 100% and 96.67% respectively. Hence by maintaining a pressure amplitude greater than 110 kPa in the first stage and 80 kPa in the second stage, a separation efficiency greater than 96% can be obtained for both the particles.

4.2 Critical particle size for acoustic particle separation with 3 μm particles

A procedure similar to the one described in the Sect. 4.1 is used for determining the critical particle size for acoustic particle separation. During the first set of simulations, input wavelength was taken as 300 μm and a constant pressure amplitude (I) of 100 kPa was applied in the first stage. An inlet mass flow rate of 8.33e−09 kg/s was taken as inlet boundary condition. The separation efficiency was then calculated for diameter of particles varying from 5 to 10 μm at different second stage pressure amplitudes (II). Figure 8 illustrates the variation of separation efficiency with second stage pressure amplitude for particle of different sizes.

From Fig. 8, it is observed that both 3 μm and 7 μm particles can be separated effectively with a separation efficiency greater than 80% at 90 kPa. However, there is no optimum pressure amplitude at which 3 μm and 6 μm or 3 μm and 5 μm are separated effectively.

The separation efficiency obtained for 3 μm particles can be further improved by increasing the pressure amplitude (I) in the first stage. Figure 9 shows the variation

of separation efficiency with second stage pressure amplitude (II) while the pressure amplitude (I) in the first stage was maintained at 120 kPa.

From Fig. 9, it can be observed that both 3 μm and 6 μm particles have a separation efficiency greater than 80% at 110 kPa pressure amplitude. However, the variation between the separation efficiency of 3 μm and 5 μm particles increased with the increase in first stage pressure amplitude. Hence, by maintaining a pressure amplitude greater than 120 kPa in the first stage and 110 kPa in the second stage the critical size of the particle that can be separated with 3 μm particles is 6 μm.

4.3 Effects of flow rate on separation efficiency

During the first set of simulations, the wavelength, pressure amplitude in the first and second stage were set to 300 μm, 120 kPa and 110 kPa respectively. Particles of 3 μm and 6 μm diameter were selected for the simulation as it was observed from Sect. 4.2 that 6 μm is the critical size that can be separated with 3 μm. The separation efficiency for the particles was then calculated for flow rates varying from 8.33e−09 to 8.33e−08 kg/s. The variation in the separation efficiency as a function of flowrate is illustrated in Fig. 10.

From Fig. 10, it is observed that as the flow rate is doubled the separation efficiency of 6 μm particles decreases from 86.67 to 13.33%, while it decreases from 93.33 to 66.67% for 3 μm particles. The variation in separation efficiency for 6 μm particles is greater than that of 3 μm particles. This is because, as the flow rate is doubled,

Fig. 8 Variation of separation efficiency with pressure amplitude (II)

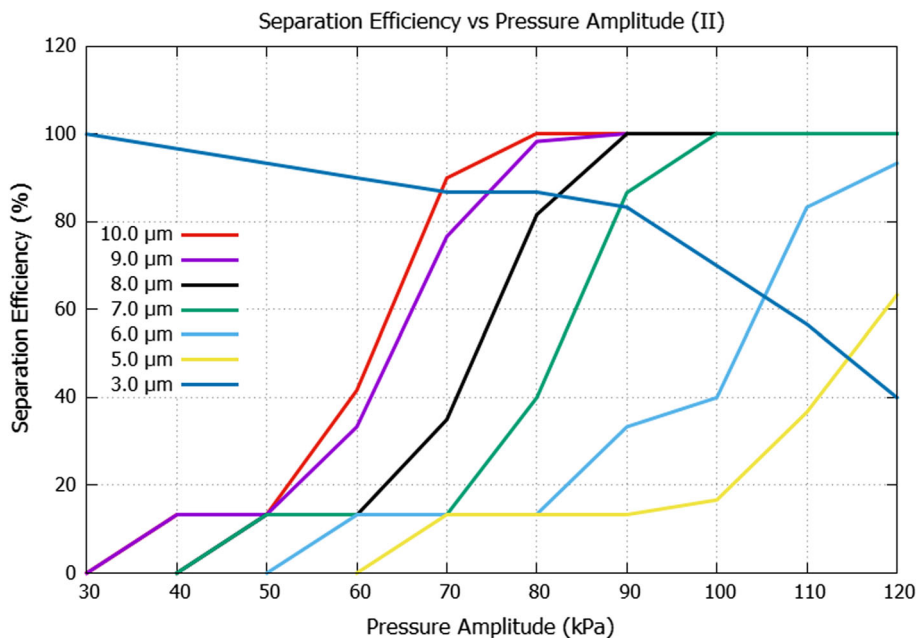
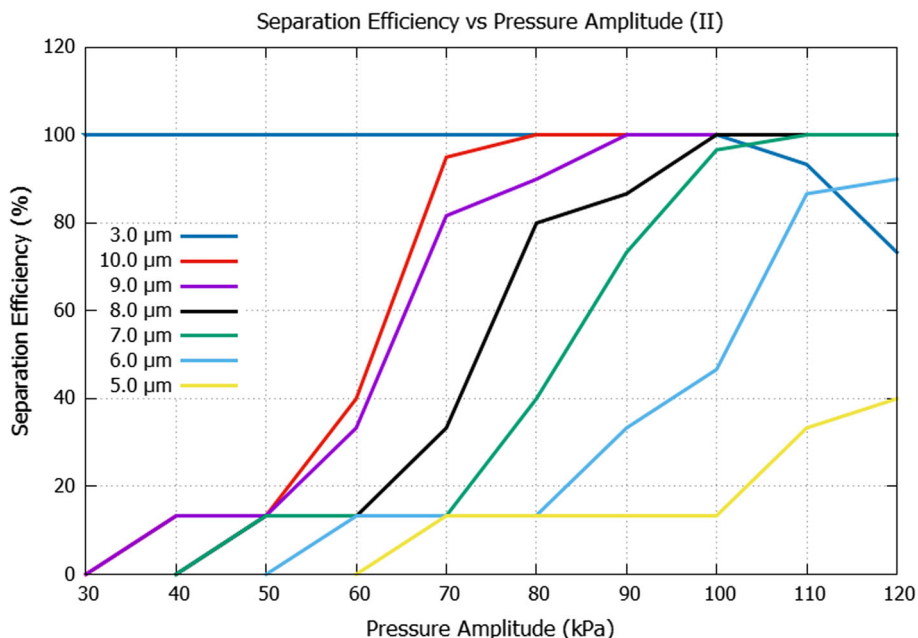


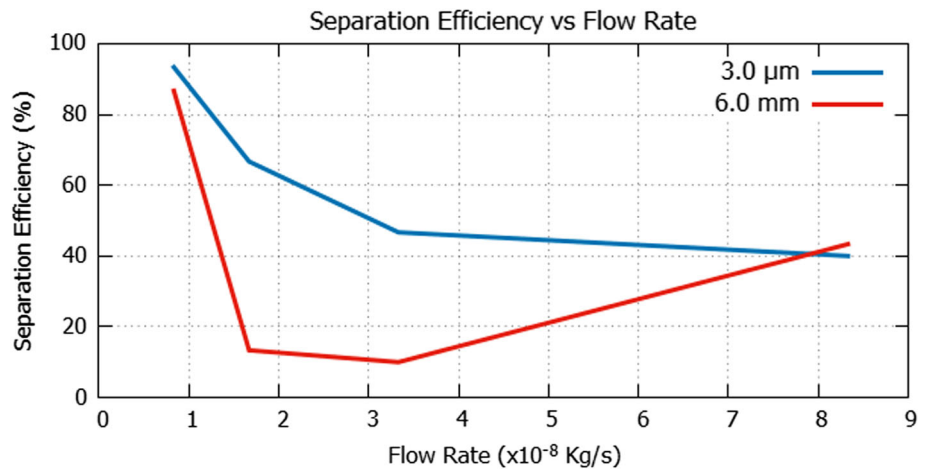
Fig. 9 Variation of separation efficiency with pressure amplitude (II)



6 μm particles spend less time in the second stage thereby reducing the separation from 3 μm particles. However, for 3 μm particles, spending less time in second stage would decrease the deviation from their respective outlet resulting in higher separation efficiency than 6 μm particles. As the flow rate is increased from 1.67e−08 to 8.33e−08 kg/s the separation efficiency for 3 μm particles gradually decreases. This is expected as the concentration of 3 μm particles at the center of the channel decreases with the increase in flow rate. As a result, the number of 3 μm particles decreases at its respective outlet.

For 6 μm particles, as the flowrate increases from 3.33e−08 to 8.33e−08 kg/s, the concentration of particles at the center of the channel decreases. This results in an easier sorting of particles in the second stage. Due to this separation efficiency of 6 μm particles increases as illustrated in Fig. 10. As 6 μm is the critical size of the particles that can be separated with 3 μm, the separation efficiency for particles of larger diameter will be higher than that of 6 μm particles represented in Fig. 10.

Fig. 10 Separation efficiency as a function of flow rate



4.4 Effect of interdigital transducer (IDT) length on separation efficiency

One of the most important parameters that decides the efficiency of the separation is the length of IDTs. The optimum length of the IDTs required for efficient separation of particles is found by performing simulations for various IDTs lengths. During the simulation, the wavelength, the pressure amplitude in the first and second stages were set to 300 μm , 120 kPa and 110 kPa respectively. Particles of 3 μm and 6 μm were selected for the simulation and a flowrate of $8.33\text{e}-09$ kg/s was taken as the inlet condition. As the design concept is of a two-stage SSAW particle separator, the separation efficiency is found by varying the length of one stage at a time while keeping the other constant.

In the first set of simulations, the length of second stage IDTs is maintained constant at 1.7 mm while for the first stage it is varied from 5.7 to 9.7 mm. The obtained

separation efficiency results as a function of IDTs length is illustrated in Fig. 11.

From Fig. 11 it is observed that the separation efficiency of 3 μm particles gradually increases with the increase in IDTs length and reaches 100% at 8.7 mm. This behavior is expected as the concentration of 3 μm particles increases at the center of the channel with the increase in length of first stage IDTs. This results in an increased separation efficiency as the deviation of 3 μm particles from its respective outlet decreases.

As observed from Fig. 11, the separation efficiency of 6 μm particles remains more or less the same with the change in first stage IDTs length. The reason for this is, IDTs of length 5.7 mm is sufficient enough for 6 μm particles to move to the center of the channel. From the above results it can be observed that the length of first stage IDTs doesn't really effect the efficiency of 6 μm particles. But to obtain the optimum separation efficiency for both the particles, one should maintain IDTs of length greater than 8.7 mm in the first stage.

Fig. 11 Separation efficiency as a function of first stage IDTs length

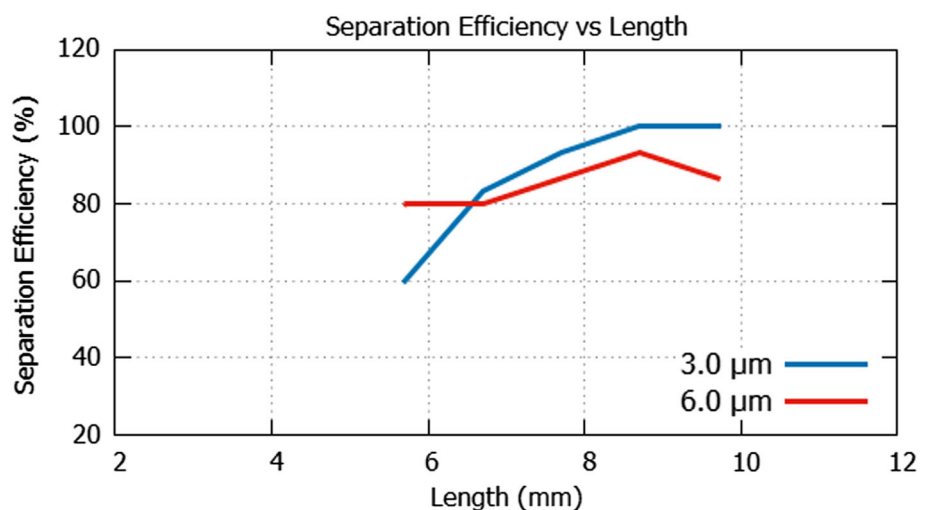
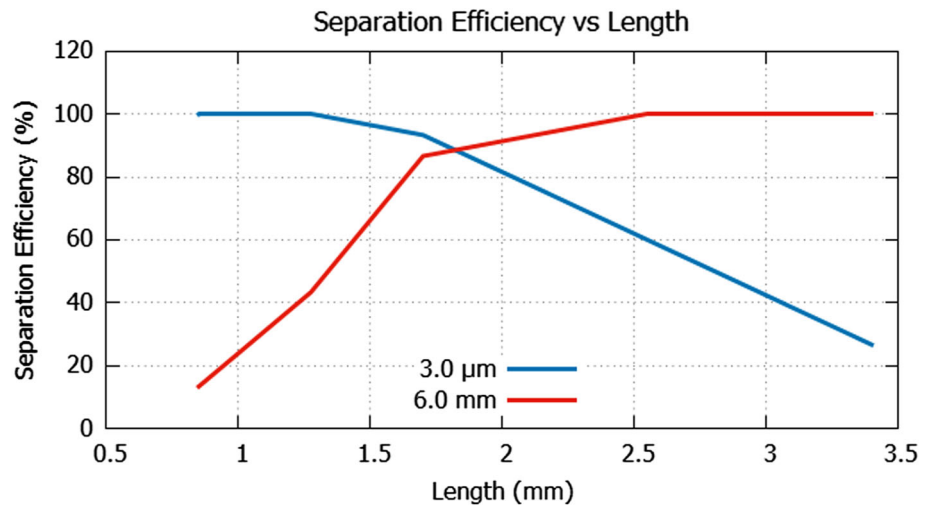


Fig. 12 Separation efficiency as a function of second stage IDTs length



During the second set of simulations, IDTs length in the first stage was set to 7.7 mm and the length in the second stage was varied from 0.85 to 3.4 mm. Figure 12 illustrates the obtained separation efficiency results as a function of IDTs length.

From Fig. 12, The optimum length of second stage IDTs was found to be 1.7 mm where both 3 μm and 6 μm particles have an efficiency of 93.33% and 86.67% respectively. For IDT's of length less than the ideal parameter, both particle sizes spend less time in the second stage. Due to this, the separation of 6 μm particles from 3 μm decreases. For IDT's of length more than the ideal value, both the particles experiences ARF for a relatively longer period. As a result, the deviation of 3 μm particles from its respective outlet increases causing a decrease in separation efficiency. These two phenomena of the particles can be

observed in Fig. 12, where there was no significant separation of particles for IDTs of length less than 1.5 mm or greater than 2.5 mm. Hence by maintaining second stage IDTs length of 1.7 mm and first stage IDTs length greater than 8.7 mm one could obtain high separation of particles.

4.5 Effect of transducer wavelength on separation efficiency

For determining the effect of transducer wavelength on separation efficiency, numerous simulations have been carried out by taking the pressure amplitudes in the first and second stage to be 120 kPa and 110 kPa respectively. The simulations were performed for 3 μm and 6 μm particles for a constant flowrate of $8.33e-09$ kg/s. The

Fig. 13 Separation efficiency as a function of first stage wavelength

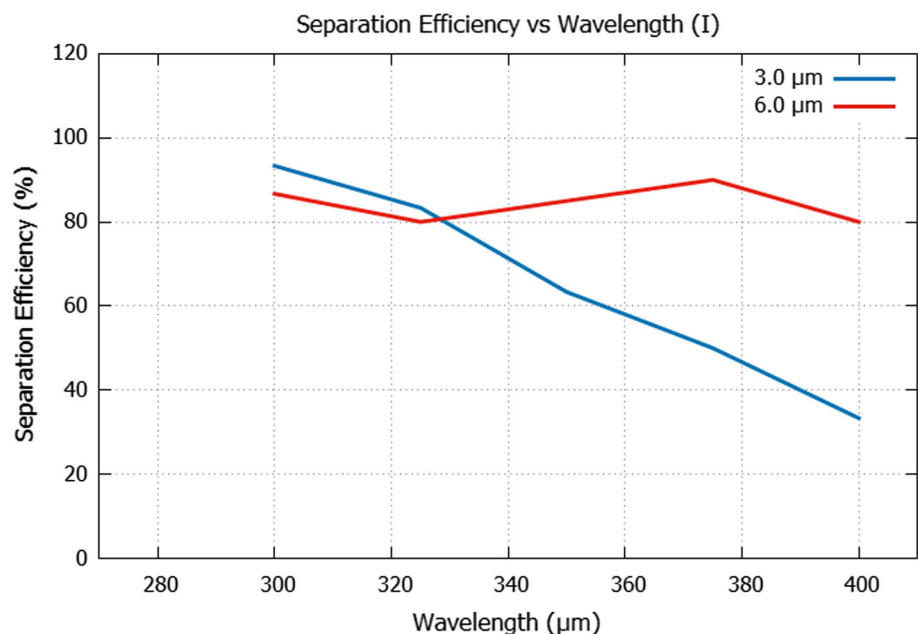


Fig. 14 Variation in ARF as a function of particle position (x) for different wavelengths

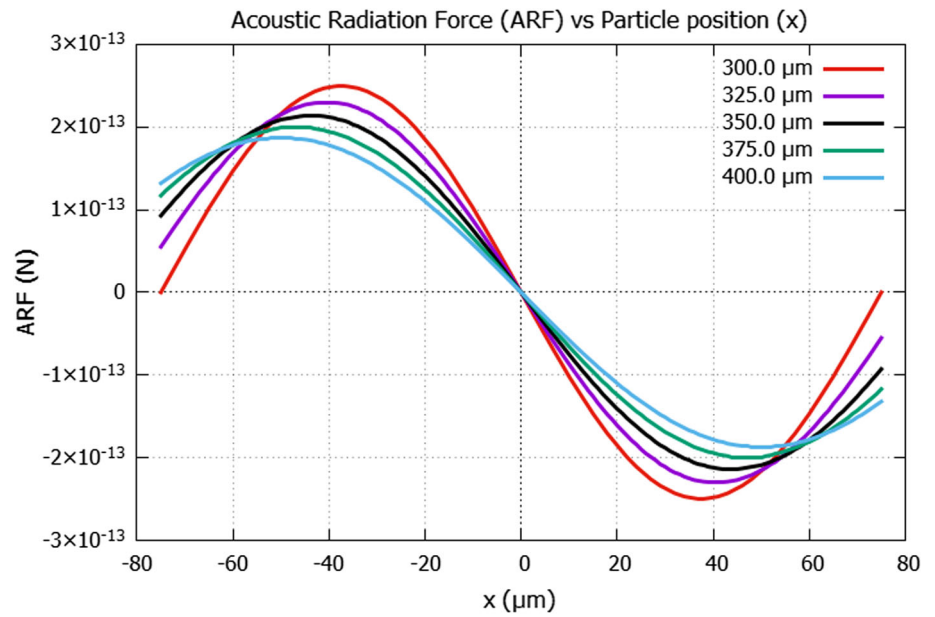
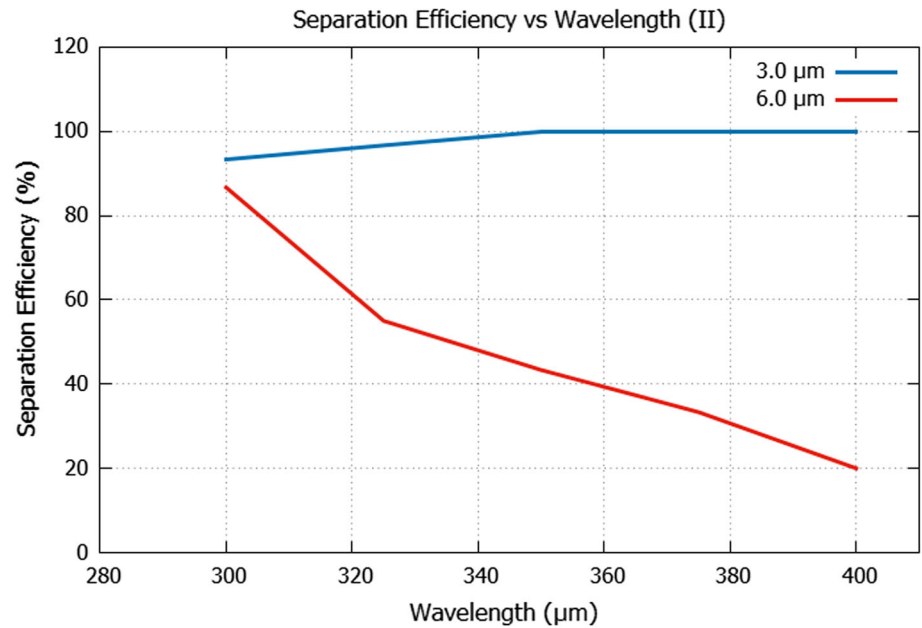


Fig. 15 Separation efficiency as a function of second stage wavelength



separation efficiency is then calculated by varying the wavelength at one stage while keeping the other constant.

In the first set of simulations, the wavelength in the first stage was varied from 300 to 400 μm while for the second stage it was maintained constant at 300 μm. The obtained separation efficiency as a function of wavelength (I) in the first stage is illustrated in Fig. 13.

From Eq. 1, ARF on a particle is inversely proportional to the wavelength generated by the IDT's. Hence the magnitude of ARF on the particles decreases with the increase in wavelength. Due to this, the separation efficiency of 3 μm particles reduces by 64.3% as the

wavelength increases from 300 to 400 μm as illustrated in Fig. 13. This variation in ARF experienced by 3 μm particles in the first stage as a function of particle position (x) for different wavelengths is illustrated in Fig. 14. For 6 μm particles, as the wavelength increases, the variations observed in the separation efficiency is less than that of 3 μm particles. The reason for this is, a wavelength of 300 μm in the second stage is high enough to separate the particles effectively.

During the second set of simulations, the wavelength in the first stage was maintained constant at 300 μm while for the second stage it varied from 300 to 400 μm. The

obtained separation efficiency as a function of wavelength (II) in the second stage is illustrated in Fig. 15.

From Fig. 15, it can be observed that the optimal wavelength in the second stage for the effective separation of particles is 300 μm . Hence by maintaining a wavelength of 300 μm in both the stages, effective separation of particles can be achieved.

5 Conclusions

In this study, a simulation model which demonstrates the particle separation by acoustic radiation force have been developed using ANSYS® Fluent. Through theoretical and simulation data, the accuracy of the simulations has been analyzed and it is found to have an error less than 4%. As the pressure amplitude in the first and second stage is increased to 80 kPa and 110 kPa respectively, the optimization study performed have found to enhance the separation efficiency over 96% for both 10 and 3 μm particles. Also, the critical size polystyrene of particles that can be separated with 3 μm was found to be 6 μm . The findings in the present work will help in designing SSAW driven microfluidic devices and in increasing the efficiency of particle separation. Although the present work concentrates on the separation of polystyrene particles, it can also be extended for particles of any type.

References

- ANSYS® Academic Research (2017) Release 18.1 ed. vol. fluent user's guide. ANSYS Inc, Canonsburg
- Chen Y et al (2015) Simulation of avascular tumor growth by agent-based game model involving phenotype-phenotype interactions. *Sci Rep* 5:17992
- Ding X et al (2012) Standing surface acoustic wave (SSAW) based multichannel cell sorting. *Lab Chip* 12(21):4228–4231
- Ding X et al (2013) Surface acoustic wave microfluidics. *Lab Chip* 13(18):3626–3649
- Guldiken R et al (2012) Sheathless size-based acoustic particle separation. *Sensors* 12(1):905–922
- Guo F et al (2016) Three-dimensional manipulation of single cells using surface acoustic waves. *Proc Natl Acad Sci* 113(6):1522
- Hu J (2013) Ultrasonic micro/nano manipulations. World Scientific, Singapore, p 268
- Jo MC, Guldiken R (2012) Active density-based separation using standing surface acoustic waves. *Sens Actuators A* 187:22–28
- Jo MC, Guldiken R (2013) Dual surface acoustic wave-based active mixing in a microfluidic channel. *Sens Actuators A* 196:1–7
- King LV (1934) On the acoustic radiation pressure on spheres. *Proc R Soc Lond Ser A Math Phys Sci* 147(861):212
- Laurell T, Petersson F, Nilsson A (2007) Chip integrated strategies for acoustic separation and manipulation of cells and particles. *Chem Soc Rev* 36(3):492–506
- Li P et al (2015) Acoustic separation of circulating tumor cells. *Proc Natl Acad Sci USA* 112(16):4970–4975
- Liu S et al (2017) Investigation into the effect of acoustic radiation force and acoustic streaming on particle patterning in acoustic standing wave fields. *Sensors (Basel, Switz)* 17(7):1664
- Plouffe BD, Murthy SK, Lewis LH (2015) Fundamentals and application of magnetic particles in cell isolation and enrichment. *Rep Prog Phys Phys Soc (G B)* 78(1):016601
- Shi J et al (2009) Continuous particle separation in a microfluidic channel via standing surface acoustic waves (SSAW). *Lab Chip* 9(23):3354–3359
- Xiong G et al (2011) Simulation of blood flow in deformable vessels using subject-specific geometry and spatially varying wall properties. *Int J Numer Methods Biomed Eng* 27(7):1000–1016
- Yosioka K, Kawasima Y (1955) Acoustic radiation pressure on a compressible sphere. *Acta Acust United Acust* 5(3):167–173
- Zhang J et al (2014) Multi-scale patterning of microparticles using a combination of surface acoustic waves and ultrasonic bulk waves. *Appl Phys Lett* 104(22):224103

Publisher's Note Springer Nature remains neutral with regard to jurisdictional claims in published maps and institutional affiliations.